# Printing Stable Liquid Tracks on a Surface with Finite Receding Contact Angle

Wen-Kai Hsiao,* Graham D. Martin, and Ian M. Hutchings

Department of Engineering, IfM, University of Cambridge, 17 Charles Babbage Road, Cambridge CB3 0FS, United Kingdom

Ⓢ Supporting Information

ABSTRACT: We have used high-speed imaging to study the formation of liquid tracks on a surface with nonzero receding contact angle, by the sequential deposition of liquid drops. For small drop spacing we found good agreement with the track morphology predicted by an existing line stability model. In addition, we confirmed definitively the preferential drop-to-bead fluid flow and the predicted drop spreading variation in the scalloped line and paired bead formation regimes. However, we found that without accounting for drop impact inertia, the model underestimated the maximum drop spreading radii and, hence, the instantaneous track width. In addition, the printed track became stable at larger drop spacing, in contrast to the expected behavior. We believe that the destabilizing effect of a receding contact line may be minimized when track radii, as predicted by volume conservation and drop–bead coalescence dynamics, converge as the drop spacing increases. An increase in viscous dissipation and a reduction of the capillary-driven flow may be the additional stabilization mechanisms. The latter may also be responsible for achieving a stable and symmetrical track when printing with a shorter interval (higher print frequency) at a given drop spacing.
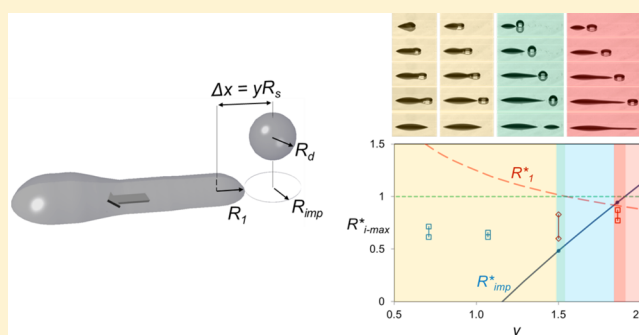
INTRODUCTION

With the current advances in 3-D printing and printed electronics applications, functional ink-jet printing has attracted significant research and development efforts. In contrast to graphical applications in which the printed images are formed by discrete ink deposits derived from single or in some cases multiple drops, printed functional patterns are often continuous features, such as lines or tracks, formed by the merging of individually deposited liquid drops on the surface. The functionality of these printed patterns, be it the conductivity of a printed circuit track or the structural integrity of a 3-D printed object, can depend strongly on their geometrical quality. In both cases, discontinuities in the deposited material can be disastrous for their performance. A good understanding of how continuous features are formed is, therefore, essential for optimizing many ink-jet-based digital fabrication processes.

The stability of an elongated bead of liquid on a surface has been a well-studied subject.[1−6] Considering a liquid line with a constant circular cross section on a solid surface, Davis noted that on the basis of a linear stability analysis the line is always unstable when either the contact line is free to move or the contact angle is greater than $\pi/2$ when the line is pinned.[1] Schiaffino and Sonin confirmed Davis's conclusion with experiments in which they printed molten wax (which gives a pinned contact line on a cold substrate) and water (with a moving contact line).[2] Focusing on the scenario where the contact line is pinned, Duineveld investigated an alternative form of line instability when the pressure-driven flow along the

liquid line is sufficiently large to transport newly deposited drops into regularly spaced bulges.[3] This bulging instability arises when too many drops are deposited too quickly: the frequency of the bulges was shown to increase with either a decrease in drop spacing or an increase in deposition rate. This is therefore relevant when a maximum stable line width is desired. However, many functional printing applications aim to create small and precise features, and hence, a minimal line width may be more relevant. Using a volume conservation model and assuming a pinned contact line, Stringer and Derby explored the lower bound of line stability when the drop spacing is just small enough to avoid scalloped edges.[4] Incorporating the finding of Duineveld, they further mapped the region of stability defined by the equilibrium contact angle, drop spacing, and print velocity.

While the work outlined above established the fundamental criteria to create a stable printed line, most previous analyses and experiments do not adequately investigate the transient dynamics of line formation. Specifically, while drop spacing and print speed (i.e., drop deposition intervals) are used to define the line stability regimes in most studies, few have investigated the dynamics between a newly deposited drop and an existing liquid bead. Soltman and Subramanian have provided a simple model to consider such dynamics. Assuming that a newly

landed drop will preferentially flow into an existing bead on contact and that the liquid–solid contact line cannot retract (zero receding contact angle), their model compares the free-spreading radius of a drop on the surface and the bead radius to determine the drop spacing threshold for the onset of scalloped lines.[5] While their concept is attractively simple and simulations were performed to support the model, no attempt was made to verify the predicted dynamics experimentally.

Furthermore, most analyses of line stability require a pinned contact line as a necessary condition. It has been argued that a pinned contact line may be regarded as the default case in functional printing,[4] since the presence of particles in the printed drop can lead to contact line pinning by the solid deposit formed as the suspending fluid evaporates.[7,8] However, drop evaporation experiments have shown that a "stick–slip" contact line motion is possible for colloidal suspensions on a surface with finite receding contact angle,[9] so this suggestion is far from definitive. Moreover, observing his printed line broke into separate beads on a surface with finite receding contact angle, Duineveld assumed assumed that the beads' noncircular footprints were due to contact angle hysteresis.[3] Subramanian and colleagues have taken advantage of this phenomenon to optimize the printing of partially wetting films[10,11] and tailored patterns.[12] Further study of the dynamics of drop–bead interaction with a nonpinned contact line will therefore certainly be relevant to a broad range of functional printing applications.

In the present study we investigated the dynamics of printed line formation by using high-speed imaging, with methods similar to those we reported previously.[13] The technique allows us to study the interaction between impacting drops and previously deposited liquid with submillisecond resolution. By printing a mixture of water and ethylene glycol to form short tracks on a surface with a finite receding contact angle, we aimed to verify the line stability mechanisms proposed by Soltman and Subramanian and to explore whether it is possible to produce a printed track with mobile contact line that is stable over the time scale of typical ink-jet printing processes.

■ THEORETICAL BASIS

As our investigation focuses on the dynamics of the drop-landing event during printed line formation, it is useful to review the dynamics of drop impact, as well as to summarize the model proposed by Soltman and Subramanian.

The postimpact spreading behavior of a submillimeter liquid drop deposited on a solid surface has been well-characterized.[13−17] Rioboo et al.[14] separated the drop deposition process into the following phases: kinematic and spreading (I), relaxation (II), and wetting/equilibrium (III). The radial expansion of the deposited drop during phase I is primarily determined by the drop impact inertia. The *maximum diameter or radius* achieved by the spreading film at the end of phase I is typically defined as D_{max} or R_{max}, respectively. Depending on the extent of the impact-driven spreading and the level of viscous dissipation, the deposited drop will either oscillate or relax during phase II and then spread under capillary forces in phase III to reach an equilibrium sessile shape with a *steady state diameter or radius* of D_s or R_s, respectively. Figure 1 shows the typical temporal evolution of a deposited drop used in the present study. Whereas phase I lasts for approximately 50 μs after impact, a further 400−500 μs is needed to dissipate the drop impact inertia in phase II. Spreading under the capillary
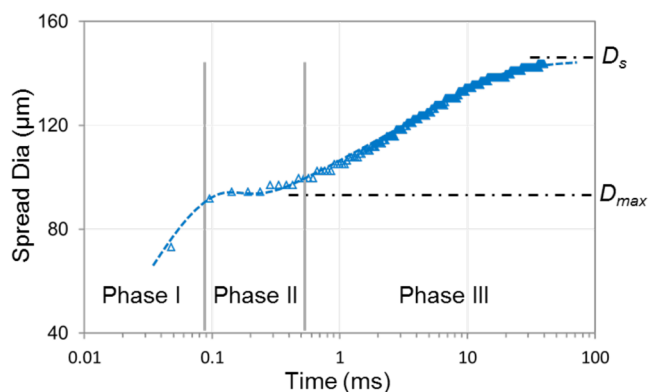

Figure 1. Temporal evolution of a typical drop used in the present study: (I) kinematic/spreading phase, (II) relaxation phase, and (III) wetting/equilibrium phase.

force, the resultant sessile drop can take up to 50 ms to approach a steady state in phase III.

After impact, the contact line of a deposited drop can advance, retract, or remain stationary. The contact line motion is often associated with a change in the contact angle at the liquid–solid–gas triple point, and there are variations of this relationship, as outlined by Davis in the context of liquid line stability[1] and comprehensively by Bourgès-Monnier and Shanahan in the context of the evaporation of a sessile drop.[18] In the case when evaporation is insignificant and the contact line motion is controlled by fluid momentum and surface tension alone, the contact angle may show hysteresis behavior; i.e., it can vary when the contact line is stationary, with distinct upper and lower limits beyond which the line will move.[19] A special case of contact angle hysteresis is when the receding contact angle is equal to 0. In this case, the contact line begins to advance at a specific critical contact angle but cannot recede.

Assuming a nonreceding contact line and that it is energetically favorable for the fluid in an overlapped drop to flow into a pre-existing liquid bead, Soltman and Subramanian developed a geometrical description of the interaction between an impacting drop and a bead formed from previously deposited drops.[5] The schematic diagram illustrating their model and the relevant parameters is shown in Figure 2. If
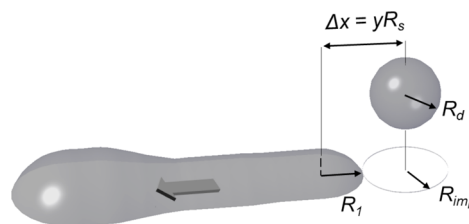
**Figure 2.** Schematic of the liquid bead formation model.

drops with radius R_d combine to form a cylindrical liquid bead on a surface, the radius of the resultant bead, R_1, is an inverse square root function of the spacing between drops Δx

$$R_1 = \sqrt{\frac{8}{3}\left(\frac{R_d^{\ 3}\psi}{\Delta x}\right)}$$

(1)

where ψ is a geometric function of the apparent static contact angle θ_s expressed as[5]

Table 1. Fluid and Interfacial Properties of 82.5/17.5 wt % Ethylene Glycol and Deionized Water Mixture on Glass

ρ (kg/m³)	μ (mPa·s)	α (N/m)	θ_s (deg)	θ_a (deg)	θ_r (deg)	ψ	R_s (μm)
1016	10	0.054	34 ± 5	44 ± 5	20 ± 5	0.26	70 ± 3
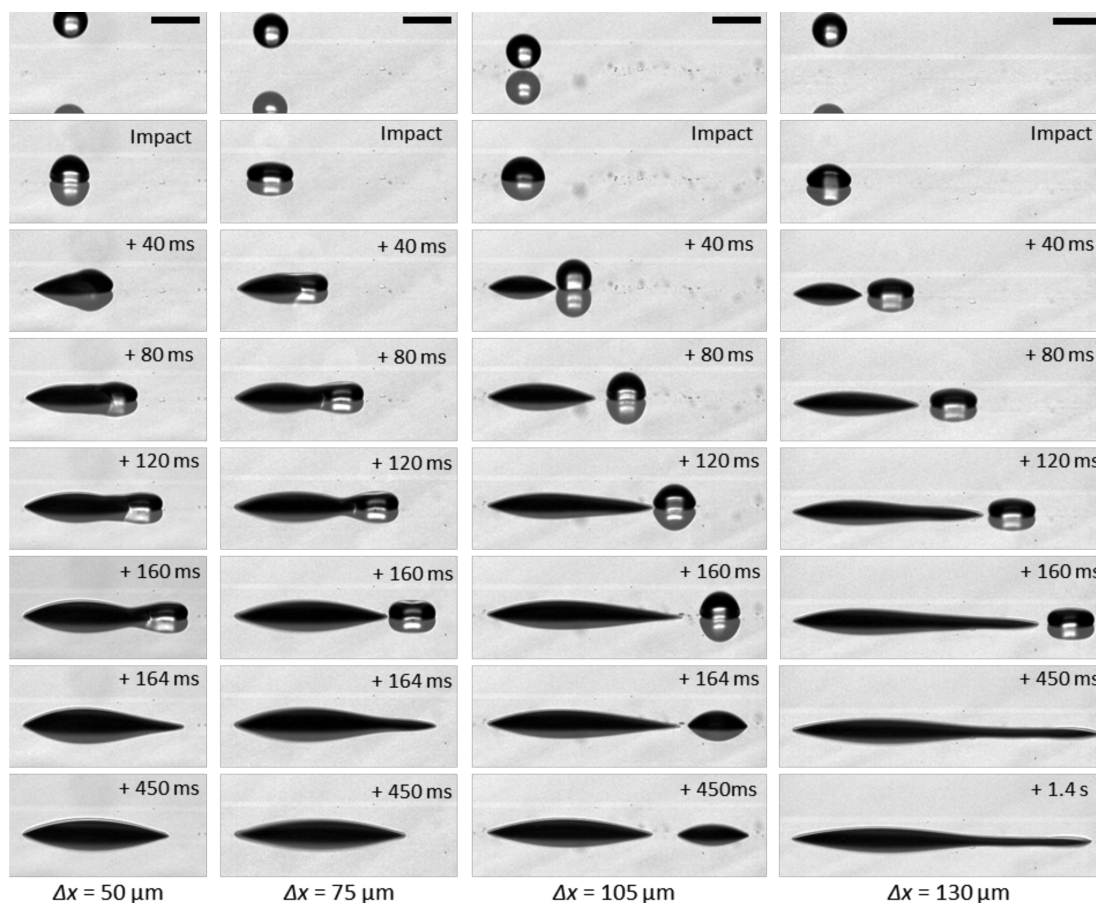
Figure 3. Track formation dynamics at different drop spacing (drop radius, R_d = 37.3 μm; interdrop time, Δt = 40 ms; scale bars indicate 100 μm).

$$\psi = \frac{\pi}{2}\left(\frac{\sin^2\theta_s}{\theta_s - \sin\theta_s\cos\theta_s}\right) \quad (2)$$

Assuming that the radius of the end of the bead is R_1, the maximum contact radius to which a newly landed drop can spread before contacting the existing bead is

$$R_{imp} = \Delta x - R_1 \quad (3)$$

R_1 decreases and R_{imp} increases as Δx grows larger, according to eqs 1 and 3. When R_{imp} becomes greater than R_1, a scalloped line is possible. As Δx increases further and R_{imp} approaches its maximum value of R_s, landed drops will start to merge in pairs before finally forming individual isolated deposits. Plotting the dimensionless radii $R_1^* = R_1/R_s$ and $R_{imp}^* = R_{imp}/R_s$ against the nondimensional drop spacing $y = \Delta x/R_s$, Soltman and Subramanian were able to identify four theoretical regimes: continuous line with straight edges, scalloped line, pairwise bead formation, and isolated drop deposition.

While Soltman and Subramanian provided simulations (Flow3D) to support their model, no empirical results were available to confirm the proposed drop–bead interaction dynamically. Although their observed final line morphology generally mapped on to the predicted regimes, qualitative adjustments were required to account for the effect of drying

and impact inertia. Furthermore, their model did not consider the effect of the fluid inflow from subsequent drops on the morphology of an existing bead, which may be significant when printing shorter tracks or attempting to minimize the bulging end effect observed by Duineveld.[3] In the present work, by visualizing the drop–bead interaction dynamics in real time and considering the case of a mobile contact line, we aimed to validate the hypotheses made in the model of Soltman and Subramanian and to broaden its application to the formation of continuous tracks by ink-jet printing on any impermeable surface.

■ MATERIALS AND METHODS

Droplets of a mixture of ethylene glycol (EG) and deionized (DI) water (82.5 wt % EG) were printed from a MicroFab print head (MJ-ABP-01-80-6MX, MicroFab Technologies) consisting of a glass capillary, surrounded by a piezoelectric driving element, which tapers to an 80 μm diameter nozzle. A custom pneumatic controller was used to control the meniscus position within the nozzle by adjusting the pressure in the fluid reservoir. A tailored bipolar waveform amplified by a dedicated controller (JetDrive III, MicroFab Technologies) was applied to produce drops with an average diameter and velocity of 74.5 μm and 1.94 m/s, respectively. The drop diameter was determined manually from individual video frames and was found to be consistent within the pixel resolution of the images (1.33 μm per pixel). The drop velocity was calculated from consecutive video frames with a known
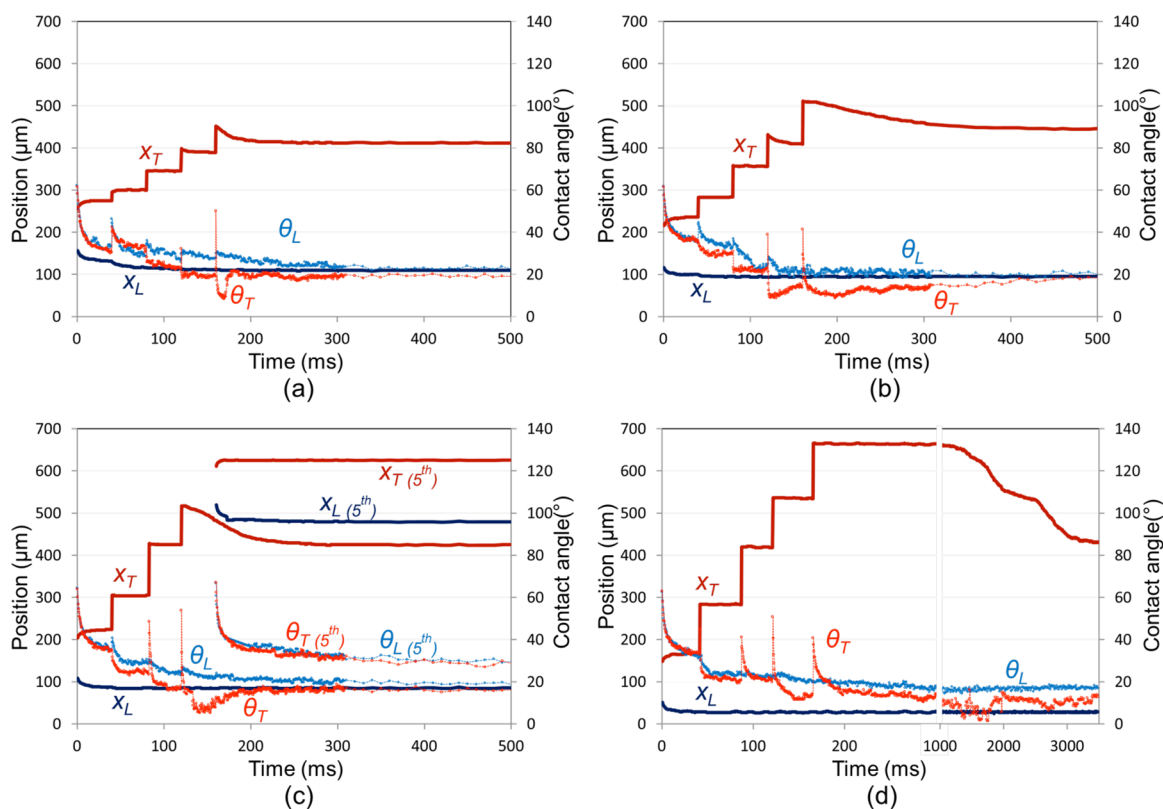
Figure 4. Dynamics of bead edge positions (X_L and X_T) and contact angles (θ_L and θ_T): (a) $\Delta x = 50\ \mu$m, (b) $\Delta x = 75\ \mu$m, (c) $\Delta x = 105\ \mu$m, and (d) $\Delta x = 130\ \mu$m.

frame rate and has a standard deviation of 0.024 m/s. The distance between the nozzle outlet and the substrate was maintained at 1.5 mm. The substrates were standard glass slides (MENZEL-GLÄSER SuperFrost, Thermo Fisher Scientific) cleaned by hand-washing in detergent, followed by rinsing sequentially with DI water, filtered acetone, and isopropyl alcohol, before final drying in an oven at 120 °C for >2 h. The fluid properties as well as the measured static, advancing, and receding contact angles on the cleaned glass surfaces, θ_s, θ_a, and θ_r, respectively, are listed in Table 1.

The printing experiments were carried out with a custom printing and imaging apparatus. The print head was mounted in a temperature-controlled holder positioned by a linear motor stage with 50 mm of travel. The substrates were mounted on a manual X–Y stage with a traveling range of 55 × 75 mm. The print head and substrate stages were mounted on separate pivoting bases so that the substrate was isolated from any motor stage vibration during the head movement. The separate bases also allowed both stages to pivot about the same axis so that the drop deposition and camera viewing angles can be adjusted independently. The imaging area was back-illuminated by a metal halide light source (PhotoFluor II, 89 North) equipped with a liquid light guide. The shadowgraphic image of the line formation was recorded at a resolution of 512 × 256 pixels, initially at 21 052 frames per second (fps) for up to 308 ms and then at a lower rate of 1000 fps for a further 3.5 s with a high-speed video camera (Phantom V7.3, Vision Research) equipped with high-magnification optics [12× zoom lens (Navitar) and 15× Plan Apo infinity-corrected long WD objective (Mitutoyo)]. Under the typical experimental conditions the evaporation time of an EG/DI water drop on glass was observed to be at least an order of magnitude longer than the recording period. Therefore, the effect of evaporation on the dynamics of the contact line and the contact angle was expected to be minimal.

Printed tracks were formed by traversing the print head across the substrate while it dispensed five drops at set time intervals. The drop spacing and time interval could be adjusted independently by altering the head stage speed and the drop ejection frequency. The high-speed video recordings were converted into individual images before being

processed with a custom MATLAB routine. The routine used Otsu's method[20] to determine the greyscale threshold, which identified the surfaces of the printed tracks and the locations of the air–liquid–solid triple points. Second-order polynomial curves were fitted to the liquid surfaces near the triple points in order to determine the dynamic contact angles. The measured contact angle values were then geometrically corrected for the 5° viewing angle using an approximated linear function. Due to the large amount of data in the recorded videos, the dynamics of the edge positions and contact angles were represented by the data from every 10th frame to improve clarity.

■ EFFECT OF DROP SPACING

The formation process for five-drop tracks of the ethylene glycol–water mixture deposited onto glass with different drop spacings is illustrated in Figure 3. As these images were captured with the lens axis at a nonzero angle of incidence, reflections of the liquid bead and drops in the substrate surface are visible in each frame. The drop deposition interval Δt was held constant at 40 ms as the drop spacing Δx was increased from 50 to 130 μm. For each drop spacing, printing was repeated up to 5 times and the sequence that best represented the track formation behavior was analyzed. The individual drop diameters and landing locations were determined manually to account for any variation in the ink-jet printing process, e.g., drop trajectory variation, and the drop spacing had a maximum standard deviation of 5.6 μm.

For the two smallest drop spacings of 50 and 75 μm, all the drops after the first either impacted directly onto the previously deposited bead or merged with it soon after deposition. The track shapes were distinctively asymmetric immediately after the landing of the fifth and final drops, as shown in the frames captured 164 ms after the impact of the first drops. The "heads"

or leading edges of the tracks were significantly larger, suggesting a net fluid flow from the later deposited drops into the pre-existing beads. With a slight delay after the deposition of the final drops, the "tails" or trailing edges of the tracks eventually unpinned and the contact line receded toward the left.

For $\Delta x = 105$ μm, all five drops landed on the dry surface. As shown in Figure 3, the gap between the impacting drop and the previously deposited liquid varied significantly from drop to drop, increasing from the second to the third drop but decreasing from the third to the fourth, in a fully reproducible manner. The larger gap at the impact of the fifth drop (shown in the 160 ms frame) clearly resulted from the contact line retracting, as this drop, despite spreading, never made contact with the pre-existing bead. Had printing continued beyond the fifth drop, we would have expected a new, separate bead to form on the surface, producing an interrupted track, as observed by Duineveld[3] and Soltman and Subramanian.[5]

For $\Delta x = 130$ μm, all the drops again impacted the dry surface. In this case, the drop spacing was sufficiently large that the impacting drops did not contact the pre-existing bead, even when fully extended to their maximum contact diameter $2R_{max}$. The subsequent drop–bead coalescence was therefore not affected by impact inertia, and all drops merged with the previously deposited liquid to form a single continuous track during their capillary spreading phases. Little or no contact line retraction was observed during printing, and the resulting track was stable for more than 1.4 s after printing started. However, it was still significantly asymmetric in shape with an engorged head, signifying that net fluid flow from the deposited drops into the bead had still occurred.

To study the dynamics of track formation in detail, the temporal variations of the trailing and leading edge positions, X_T and X_L, and the associated contact angles, θ_T and θ_L, are plotted in Figure 4.

For $\Delta x = 50$ and 75 μm, the second and third drops merged with the previously deposited liquid at or immediately after impact, with minimal or no retraction of the contact line. The effect of the fluid momentum from the deposited drops was evident in the early stage of track formation by the outward movement of the leading edges, signified by large increases in θ_L and small but notable decrease in X_L in both parts a and b of Figure 4, coinciding with the arrival of the second drops. Both θ_T and θ_L decreased as more drops were added to the beads, although only θ_T decreased in distinct steps as each drop arrived. For both drop spacings, θ_T approached θ_r after the deposition of the fourth drops and the trailing contact lines started to retract, signified by the decreases in X_T. However, in both cases the drop spacing was sufficiently small that the fifth drop was able to bridge the gap to the previous deposit and the track grew continuously without interruption. Retraction of the trailing contact lines continued after the deposition of the fifth drop. The rate of retraction appeared to be proportional to the difference between θ_T and θ_r (noting that the rapid reduction of X_T mirrored the large dip of θ_T after the landing of the fifth drop for $\Delta x = 50$ μm). Conversely, in neither case did θ_L decrease sufficiently to initiate contact line retraction, and X_L reached a minimum value soon after the deposition of the third drop.

For $\Delta x = 105$ μm, as shown in Figure 4c, the trailing contact line retracted after the deposition of the fourth drop. The retraction accelerated when θ_T dropped below θ_r and created a gap that the fifth drop was unable to bridge. We also noticed

that the step increase in X_T was less even, with a significantly larger increase after the landing of the third drop compared with that of the second and fourth drops.

Distinctly different dynamics were observed for $\Delta x = 130$ μm, as shown in Figure 4d. There was minimal or no observable contact line retraction during the intervals between the drop impacts. Both X_T and X_L remained stable for up to 1 s after the deposition of the fifth drop. Ultimately, the right track edge began to recede in a "stick–slip" fashion. While the contact line at the right bead edge was not receding during printing, θ_T was observed to vary, alternating from a step decrease after the second drop to a step increase after the third drop, and so on. This behavior differed significantly from that observed at the smaller drop spacings, in which θ_T decreased in a series of steps after the addition of each drop.
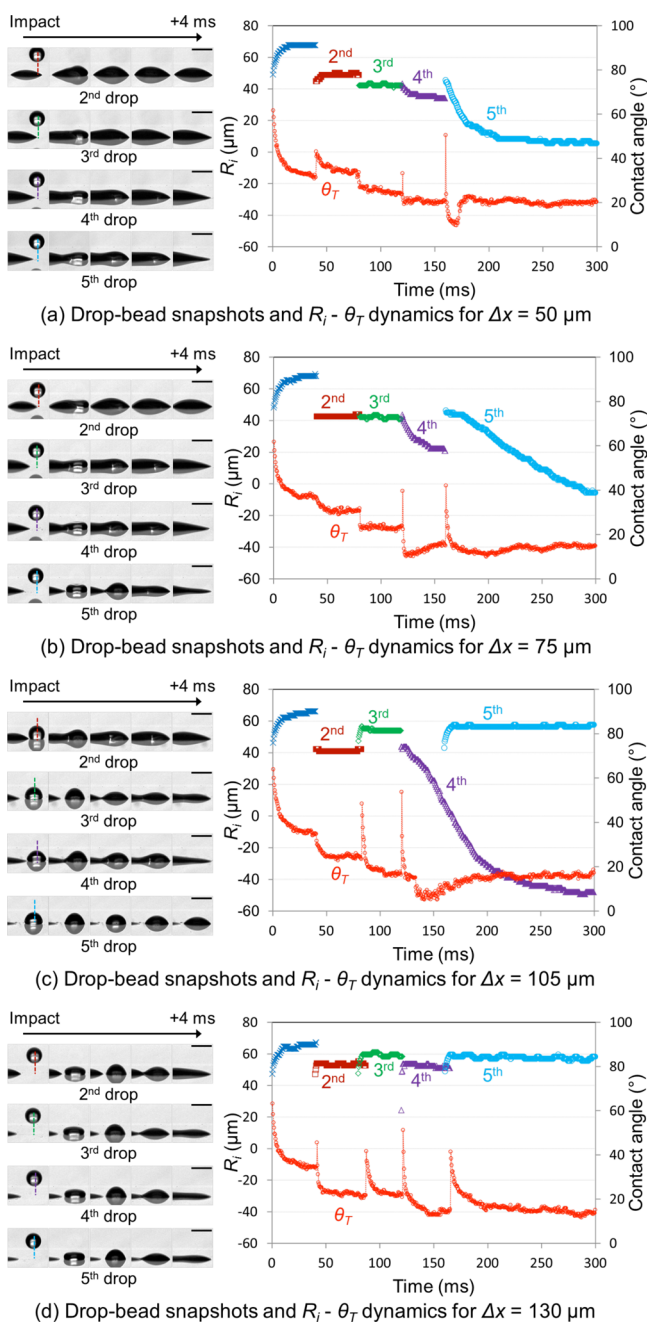
The analysis of the contact line motions and their associated contact angle dynamics suggests that there may be a fundamental change in drop spreading dynamics as Δx increases. To investigate this in the context of drop–bead interactions, we analyzed the image data to study the landing events in detail. Figure 5 shows the drop landing positions and images of the drop–bead junctions during coalescence. In addition, the instantaneous drop radii R_i, determined by the differences between X_T and the landing positions, were plotted with the associated θ_T against time. Note that the maximum value of R_i, or R_{i-max}, is equivalent to R_{imp} as defined in eq 3.

In all cases the spreading of the first drops alone allowed them to approach the final contact radius of an isolated drop, R_s. The spreading of all later drops was constrained by the interaction with the previously deposited liquid. This observation confirmed that the smaller increases of X_T observed after the second drop impacts in Figure 4a–c were results of greater spreading of the first drops rather than any variation in the landing positions.

As shown in Figure 5a for $\Delta x = 50$ μm, R_i for the drops varied as the track grew. Specifically, the second drop expanded after landing, but the radius of the third drop remained constant. The images show that the second drop landed directly onto liquid from the first drop. Therefore, its expansion was driven by undissipated impact inertia. In contrast, the third drop landed on the dry surface first and the majority of its impact inertia was dissipated to reach R_{max}. The landing event of the fourth drop was nearly identical to that of the third (hence the similar initial R_i) before contact line retraction, when θ_T dropped close to θ_r. As the drop–bead gap was increased by this retraction, the fifth drop was able to reach a greater R_i on impact before a large fall in θ_T brought on a rapid retraction.

The dynamics of R_i for the drops with $\Delta x = 75$ μm, as shown in Figure 5b, were mostly similar to the behavior with $\Delta x = 50$ μm. The main differences were the lack of expansion after impact of the second drop and a slower retraction of the fifth drop. Both observations are consistent with the effects of the greater dissipation of drop inertia on the surface and the longer time needed for the liquid to flow across the larger distances.

For $\Delta x = 105$ μm, R_i for successive drops varied upward and downward, as shown in Figure 5c. The drop spacing was just enough for the second drop to contact the liquid from the first drop immediately after reaching its R_{max}. As the spreading of the second drop was arrested close to R_{max}, the third drop had additional surface on which to spread beyond R_{max} under capillary force before contacting the previously deposited liquid. The greater expansion of the third drop, conversely, limited the

(a) Drop-bead snapshots and R_i - θ_T dynamics for $\Delta x = 50\ \mu m$

(b) Drop-bead snapshots and R_i - θ_T dynamics for $\Delta x = 75\ \mu m$

(c) Drop-bead snapshots and R_i - θ_T dynamics for $\Delta x = 105\ \mu m$

(d) Drop-bead snapshots and R_i - θ_T dynamics for $\Delta x = 130\ \mu m$

Figure 5. Snapshots of drop−bead junction up to 4 ms postimpact with dynamics of drop spreading radius and contact angle (R_i and θ_T); scale bars indicate 100 μm.

spreading of the fourth drop. If the fourth drop did not retract before the landing of the fifth drop, we would presumably see this pattern of alternating values of R_i continued indefinitely.

For $\Delta x = 130\ \mu$m, the drop spacing was sufficiently large that all the drops spread under capillary force before contacting the existing drop or bead, as shown in the images of Figure 5d. Therefore, the extents of spreading for the second and fourth drops were notably greater than in the previous case. While R_i still alternated up and down, as described above, the magnitude of this effect was approximately halved as a result. Although θ_T spiked at the landing of the second and fourth drops, subsequent drops never brought it close to θ_r as observed for the smaller drop spacing. Significantly, the curvature near the right bead edge, as shown in the images, never became concave

during the relaxation of θ_T. As a concave local curvature always preceded contact line retraction at the smaller drop spacing, we believe that such a feature directly correlated to a decrease in drop-to-bead flow, which could make a significant contribution to the track stability.

EFFECT OF DROP DEPOSITION INTERVAL

The empirical evidence presented above suggests that track formation and stability are at least partly related to the process of liquid flow from the impacting drops to the pre-existing bead. While no analytical solution is available to predict this flow, its direction and magnitude are often approximated by the pressure variation along a nonuniform track. Duineveld has described schematically the growth of a track-end bulge as a result of fluid flow driven by the higher pressure at the drop landing end due to its extra curvature (smaller radius).[3] This suggests that by reducing the curvature difference we may be able to reduce the drop-to-bead flow and improve the track stability and symmetry. One potential approach is to reduce the drop deposition interval in order to minimize the difference between the shapes of sequentially deposited drops during their coalescence.

Two tracks formed with the same drop spacing ($\Delta x = 130\ \mu$m) but with different deposition time intervals of 40 and 1 ms are shown on the left and right, respectively, of Figure 6. For


$\Delta x = 130\ \mu m$ $\Delta t = 40\ ms$ $\Delta x = 130\ \mu m$ $\Delta t = 1\ ms$
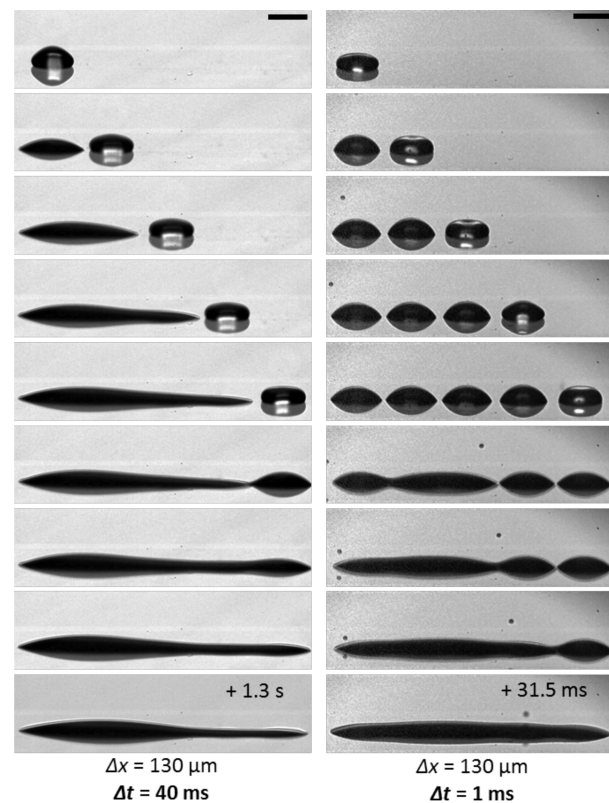
Figure 6. Effect of drop deposition intervals (Δt) on printed track morphology; scale bars indicate 100 μm.

the shorter deposition interval, shown on the right in Figure 6, all the drops formed individual sessile deposits before merging. In addition, merging did not occur first between the earliest pair of drops (the first and second drops). Instead, the second and the third drops merged first, quickly followed by the first drop, before they joined up with the fourth and fifth drops in

sequence. As no preferential fluid flow direction was established during track formation, the resultant track geometry was significantly more symmetrical than that of the track formed with the longer intervals (Figure 6, left).

DISCUSSION

Since the average R_s for these liquid drops on glass was approximately 70 μm, the nondimensional drop spacing, y, in these experiments ranged from 0.71 to 1.86. As shown in Figure 7, we were able to map the printed track morphology and
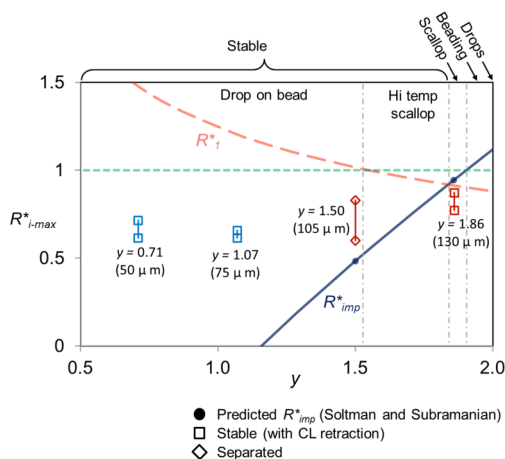
Figure 7. Experimental results mapped onto line stability regimes and the dimensionless extent of drop spreading before bead contact, R^*_{imp}, as defined by Soltman and Subramanian; y and R^*_{i-max} are dimensionless forms of drop spacing and maximum value of R_i, respectively.

values of the dimensionless R^*_{i-max} ($=R_{i-max}/R_s$) of the later drops (second to fifth drops) onto the regime map proposed by Soltman and Subramanian. For $\Delta x = 50$ and 75 μm ($y = 0.71$ and 1.07), our observations agree with their prediction that forming a continuous track is possible in this regime. Given that our liquid showed a nonzero θ_r on glass, the retractions of the trailing contact lines during and after track formation were expected and consistent with their hypothesis of a preferential drop-to-bead fluid flow. However, the average values of R^*_{i-max} were significantly greater than the values of R^*_{imp} predicted by the model and plotted on the graph. Soltman and Subramanian conceded that while their model was effective in qualitatively predicting line morphology, it may not be sufficient to predict dimensions such as line width, due to effects such as impact inertia, which were not accounted for.[5] Our high-speed imaging results clearly corroborate their view by demonstrating that during track printing, the initial, often maximum, spreading of a deposited drop is influenced by impact inertia in addition to drop spacing.

For $\Delta x = 105$ μm ($y = 1.50$), we found a closer agreement between the experimental R^*_{i-max} and the predicted R^*_{imp}. In addition, the coalescence dynamics resulting in the step difference between R^*_{i-max} of the second–fourth and third–fifth drops matches the pairwise bead formation mechanism as proposed by Soltman and Subramanian.[5] Due to the receding contact line, our printed track assumed a separated bead morphology instead of a stable or slightly scalloped track as predicted. However, it is easy to imagine a scalloped formation arising from the pairwise coalescence if the contact line is pinned rapidly, e.g., for a colloidal fluid that dries quickly.

The most intriguing comparison between our results and the model arises for $\Delta x = 130$ μm ($y = 1.86$). While all tracks printed at smaller Δx exhibited the destabilizing effect of the receding contact line, at this spacing we observed instead a stable track with well-matched R^*_{i-max} and R^*_{imp}. Although the track ultimately contracted after more than 1 s, the period of stability was an order of magnitude longer than for tracks printed with smaller Δx, signifying a change in the underlying interaction.

One potential explanation arises from how R^*_l and R^*_{imp} were determined. Specifically, whereas R^*_l was determined on the basis of volume conservation, which requires a mobile contact line, a nonreceding contact line is a prerequisite for determining R^*_{imp}, as proposed by Soltman and Subramanian. The difference in the assumed state of the contact line may explain the tendency for our experimental results, based on a receding and mobile contact line, to be consistently greater than R^*_{imp} and approaching R^*_l instead. At $\Delta x = 130$ μm ($y = 1.86$), the predicted values of R^*_{imp} and R^*_l converge, and therefore, the effect of the receding contact line is minimal.

On the basis of the observation of the drop–bead coalescence dynamics, another stabilization mechanism may also be involved. As shown in the images in Figure 5d, the neck regions during coalescence for $\Delta x = 130$ μm were considerably thinner than those with smaller drop spacings. For Poiseuille flow in a liquid film on a plane, the viscous pressure loss per unit length along the neck follows

$$\Delta P_l \propto \frac{\mu U}{h^2} \tag{4}$$

where μ, U, and h are dynamic viscosity, flow velocity, and film thickness, respectively. Therefore, a decrease in the film thickness will increases the pressure loss in the neck region and may reduce drop-to-bead fluid flow and stabilize the printed track.

Whereas the internal fluid flow between a liquid bead and a deposited drop appears to affect the stability of a printed track, it may also represent an opportunity to optimize track geometry. As, according to Duineveld's model, the internal fluid flow in a liquid bead is primarily a function of the regional curvature differences, reducing or tailoring such differences should offer us control over the internal fluid flow and, as a result, the morphology of the printed tracks. This hypothesis is supported by the observation that when drops with similar sessile shapes coalesced, they formed a stable track with symmetrical morphology, as shown in Figure 6 for drops deposited at 1 ms intervals. Although this conclusion is preliminary and so far only tested at one drop spacing, albeit a more representative one as the effect of the receding contact line appeared to be minimal, this may be a fertile area for future investigation.

Although we have discussed separately the effects of viscous dissipation at the neck region and curvature variation, it is likely that both operate together to affect the stability and geometry of a printed track. In addition, by approximating the neck region as an infinite thin film and considering only the profile curvature of the drop–bead junction, we risk oversimplifying the complexity of the drop–bead interaction. Although quantifying this interaction is beyond the scope of the present work, it may be an interesting area to explore in detail. Specifically, a future area of interest would be to observe both bottom and side profiles simultaneously during printing to define the drop–bead junction curvature in three dimensions

and quantify its correlation to the internal fluid flow using techniques such as holographic imaging of seeding particles in the fluid.

CONCLUSIONS

We have carried out a series of high-speed imaging experiments to study the dynamics of liquid track formation on a surface with a nonzero receding contact angle, as typically observed in practical applications. We explored the validity of the line stability model proposed by Soltman and Subramanian. We found that at small drop spacings, where the deposited drops coalesced during their early inertia-driven and relaxation spreading phases, the tracks were potentially stable, as predicted by the model. The tracks were ultimately destabilized by contact line retraction during and after printing, but the uniform direction of retraction confirmed the hypothesis of a preferential fluid flow from the landing drops to the pre-existing liquid bead. Furthermore, we also confirmed the pairwise variation of the maximum drop spreading radii predicted by the model. Although the model appears to predict the track formation dynamics and its mechanism of destabilization well, our results showed that, without considering the effect of drop impact inertia, it significantly underestimates the spreading of the deposited drops and, hence, underestimates the instantaneous width of the track as it grows. The best agreement between our results and the model prediction occurred at the predicted transition from continuous to scalloped line. A good match was expected as at this drop spacing a deposited drop can dissipate its impact inertia fully on the surface before coming into contact with the previously deposited bead and the effect of the receding contact line is minimal. For greater drop spacing, we found evidence of a slower drop-to-bead fluid flow, which stabilized the printed track. The slower flow was proposed to be caused either by an increase in viscous dissipation in the thinner neck region or by a reduction in the driving pressure due to the smaller curvature variations between the deposited drops and the previously deposited liquid bead. The latter hypothesis found good support from the observation of stable and symmetrical tracks printed with short time intervals, which allow similarly shaped drops to coalesce with minimal curvature variations in the neck regions. The effect of printing interval, independent of drop spacing, on track stability may have significant research and practical implications and should be investigated further.

ASSOCIATED CONTENT

Ⓢ Supporting Information

Videos of track printing at a drop spacing of 50, 75, 105, and 130 μm in AVI format. These materials are available free of charge via the Internet at http://pubs.acs.org.

AUTHOR INFORMATION

Corresponding Author

*E-mail: wkh26@cam.ac.uk.

Author Contributions

The manuscript was written through contributions of all authors. All authors have given approval to the final version of the manuscript.

Notes

The authors declare no competing financial interest.

ACKNOWLEDGMENTS

ABBREVIATIONS USED

EG, ethylene glycol; DI, deionized; WD, working distance; CL, contact line.

NOMENCLATURE

D_{max}	maximum diameter of a deposited drop at the end of the kinematic/spreading phase
R_{max}	maximum radius of a deposited drop at the end of the kinematic/spreading phase
D_s	steady-state diameter of a deposited drop on a surface
R_s	steady-state radius of a deposited drop on a surface
R_d	initial (spherical) drop radius
R_l (R_l^*)	end radius of a printed bead (dimensionless form)[5]
Δx (y)	drop spacing (dimensionless form)
θ_s	apparent static contact angle
ψ	a geometrical function of θ_s[5]
R_{imp} (R_{imp}^*)	maximum drop spreading radius before bead contact (dimensionless form)[5]
X_L	leading edge position of a printed track
X_T	trailing edge position of a printed track
θ_L	leading edge contact angle
θ_T	trailing edge contact angle
R_i	instantaneous radius of a deposited drop
R_{i-max} (R_{i-max}^*)	maximum value of R_i (dimensionless form)
θ_r	receding contact angle
θ_a	advancing contact angle
μ	dynamic fluid viscosity
α	liquid−air surface tension
ρ	fluid density
ΔP_l	Poiseuille flow pressure lost per unit length
U	Poiseuille flow velocity
h	Poiseuille flow film thickness

REFERENCES

(1) Davis, S. H. Moving Contact Lines and Rivulet Instabilities—1. The Static Rivulet. *J. Fluid Mech.* **1980**, *98*, 225−242.

(2) Schiaffino, S.; Sonin, A. A. Formation and Stability of Liquid and Molten Beads on a Solid Surface. *J. Fluid Mech.* **1997**, *343*, 95−110.

(3) Duineveld, P. C. The Stability of Ink-Jet Printed Lines of Liquid with Zero Receding Contact Angle on a Homogeneous Substrate. *J. Fluid Mech.* **2003**, *477*, 175−200.

(4) Stringer, J.; Derby, B. Formation and Stability of Lines Produced by Inkjet Printing. *Langmuir* **2010**, *26*, 10365−10372.

(5) Soltman, D.; Subramanian, V. Inkjet-Printed Line Morphologies and Temperature Control of the Coffee Ring Effect. *Langmuir* **2008**, *24*, 2224−2231.

(6) Ubal, S.; Grassia, P.; Campana, D. M.; Giavedoni, M. D.; Saita, F.A. The Influence of Inertia and Contact Angle on the Instability of Partially Wetting Liquid Strips: A Numerical Analysis Study. *Phys. Fluids* **2014**, *26*, 32106.

(7) Deegan, R. D.; Bakajin, O.; Dupont, T. F.; Hubert, G.; Nagel, S.R.; Witten, T.A. Capillary Flow as the Cause of Ring Stains from Dried Liquid Drops. *Nature* **1997**, *389*, 827−829.

(8) Sommer, A.P.; Rozlosnik, N. Formation of Crystalline Ring Patterns on Extremely Hydrophobic Supersmooth Substrate: Exten-

sion of Ring Formation Paradigms. *Cryst. Growth Des.* **2005**, *5* (2), 551−557.

(9) Moffat, J. R.; Sefiane, K.; Shanahan, M. E. R. Effect of TiO_2 Nanoparticles on Contact Line Stick−Slip Behavior of Volatile Drops. *J. Phys. Chem. B* **2009**, *113*, 8860−8866.

(10) Soltman, D.; Smith, B.; Kang, H.; Morris, S. J. S.; Subramanian, V. Methodology for Inkjet Printing of Partially Wetting Films. *Langmuir* **2010**, *26* (19), 15686−15693.

(11) Hongki, K.; Soltman, D.; Subramanian, V. Hydrostatic Optimization of Inkjet-Printed Films. *Langmuir* **2010**, *26* (13), 11568−11573.

(12) Soltman, D.; Smith, B.; Morris, S. J. S.; Subramanian, V. Inkjet Printing of Precisely Defined Features Using Contact-Angle Hysteresis. *J. Colloid Interface Sci.* **2013**, *400*, 135−139.

(13) Hsiao, W.-K.; Hoath, S. D.; Martin, G. D.; Hutchings, I. M. Inkjet Printing for Direct Mask Deposition in Printed Circuit Board Fabrication. *J. Imaging Sci. Technol.* **2009**, *53*, 050304.

(14) Rioboo, R.; Marengo, M.; Tropea, C. Time Evolution of Liquid Drop Impact onto Solid, Dry Surfaces. *Exp. Fluids* **2002**, *33*, 112−124.

(15) Dong, H.; Carr, W. W.; Bucknall, D.G. Temporally-Resolved Inkjet Drop Impaction on Surfaces. *AlChE J.* **2007**, *53*, 2606−2617.

(16) Jung, S. J.; Hutchings, I. M. The Impact and Spreading of a Small Liquid Drop on a Non-Porous Substrate over an Extended Timescale. *Soft Matter* **2012**, *8*, 2686−2696.

(17) Van Dam, D. B.; Le Clerc, C. Experimental Study of the Impact of An Ink-Jet Printed Droplet on A Solid Substrate. *Phys. Fluids* **2004**, *16* (9), 3403−3414.

(18) Bourgès-Monnier, C.; Shanahan, M. E. R. Influence of Evaporation on Contact Angle. *Langmuir* **1995**, *11*, 2820−2829.

(19) Dussan, E. B. On the Spreading of Liquids on Solid Surfaces: Static and Dynamic Contact Lines. *Annu. Rev. Fluid Mech.* **1979**, *11*, 371−400.

(20) Otsu, N. A Threshold Selection Method from Gray-Level Histograms. *IEEE Trans. Syst., Man, Cybern.* **1979**, *9* (1), 62−66.